On local-global hysteresis-based hovering stabilization of the DarkO convertible UAV

Florian Sansou, Luca Zaccarian

On local-global hysteresis-based hovering stabilization of the DarkO convertible UAV

Florian Sansou[1] and Luca Zaccarian[2]

***Abstract*— We characterize an input-affine model of the UAV DarkO: a convertible drone designed and developed at the Ecole Nationale de L'Aviation Civile (ENAC) in Toulouse (France). Starting from a nonlinear model available in the literature, we present an approximate input-affine nonlinear model, whose dynamics simplifies the control design task. For this simplified model, we characterize the hovering equilibria in the absence of wind, and we derive the corresponding linearized dynamics. Then present a hysteresis-based switching mechanism combining a nonlinear feedback (providing a large basin of attraction) with a linearized feedback (providing improved performance but a smaller basin of attraction). Simulation results, using the original nonlinear model, confirm the effectiveness of the proposed feedback design.**

I. Introduction

Convertible drones, within the class of hybrid Unmanned Air Vehicles (UAVs) are a compromise between two architectures : fixed wing and rotorcraft. Being equipped with a fixed wing, they have the ability to fly like an aircraft, with energy efficiency, but also to hover to maintain a position and perform vertical take-off and landing (see the comprehensive survey [1]). In recent years, due to their relevance to applications, different convertible UAV architectures have been proposed, which can arguably be classified in tilt-rotors, tilt-wings, quadruplanes and tilt-body (or tailsitter) configurations [2], [3]. These drones, like any other, share the important challenges of a cascaded attitude/displacement architecture, as well discussed, e.g., in [4]. In particular, the DarkO UAV recently developed at the Ecole Nationale de L'Aviation Civile (ENAC) in Toulouse (France) is an example of tailsitter comprising two propellers and two elevons with a bat-like architecture [5], [2], [6].

While convertible drones present several important advantages in terms of energy and maneuvrability, their control remains an active research field, due to the different flight conditions that should be considered in the control design. In particular, a large amount of works (see, e.g., [7], [3], [8], [9] and references therein) address the so-called transition control, wherein different flight modes are stabilized by known approaches (typically linearization-based solutions) and the transition among the different flight modes is the design goal. This control strategy is especially suited for tilt-wing configurations.

Research supported in part by ANR via grant HANDY, number ANR-18-CE40-0010.

[1]Florian Sansou is with the Ecole Nationale de L'Aviation Civile (ENAC), Toulouse, France. florian.sansou@recherche.enac.fr

[2]Luca Zaccarian is with the Department of Industrial Engineering, University of Trento, Italy, and LAAS-CNRS, Université de Toulouse, CNRS, Toulouse, France. zaccarian@laas.fr

With tailsitter UAVs, there is the possibility of developing a single feedback controller covering the whole operating range of the drone. This could be done using linear PID-based strategies [10], [11], even though limited effectiveness in terms of accuracy and disturbance rejection stems for the limited range of validity of the linearized models. For the DarkO drone, a model-free control technique has been used in [2], which allows avoiding the cumbersome modeling effort, but is clearly prone to the well-known improvements stemming from a careful model-aware solution. When the model is taken into account, one may rely on nonlinear dynamic inversion and incremental nonlinear dynamic inversion techniques (see, e.g., [12], [13], [14]). A further computationally expensive solution is that of nonlinear model predictive control (see, e.g., [15]) with its well-known computational related issues. Additional approaches include different linearization-based techniques, including LPV and gain scheduling control, as well as adaptive control strategies, to be designed by addressing the dynamics of the specific UAV model under consideration [14], [16], [3], [17], [16].

The work presented here is part of the approach initiated in [5], [2], [6] and related to the modeling of the DarkO drone and proposing a unified nonlinear, possibly hybrid, control scheme. The contribution of this paper is multi-fold. First, in Section II, we present an input-affine DarkO model, stemming from the results in the references above. Our model is suitable for control design. To this end, we characterize the equilibria and the linearized dynamics for hovering flight. Then in Section III, we present two feedback control laws, each one with advantages and drawbacks, and illustrate their blending through a hybrid hysteresis switching scheme. Our results are validated by high fidelity simulations on the identified model given in [5], [2].

Notation. Given two vectors $\boldsymbol{x_1}$ and $\boldsymbol{x_2}$, we often denote their juxtaposition as $(\boldsymbol{x_1}, \boldsymbol{x_2}) := [\boldsymbol{x_1}^\top \ \boldsymbol{x_2}^\top]^\top$. Given any vectors $\boldsymbol{u}, \boldsymbol{v} \in \mathbb{R}^3$, the skew-symmetric matrix $[\boldsymbol{u}]_\times$ satisfies $[\boldsymbol{u}]_\times \boldsymbol{v} = \boldsymbol{u} \times \boldsymbol{v}$. Symbol I denotes the identity matrix of appropriate dimensions.

II. Model of the DarkO UAV

The DarkO UAV, designed and developed at the Ecole Nationale de l'Aviation Civile (ENAC) in Toulouse (France), is a clear example of convertible UAV with a so-called tail-sitter architecture. DarkO is assembled from multiple 3D printed Onyx parts (a highly robust material comprising omnidirectional carbon fibers). Its actuators consist in two propellers symmetrically placed at the front of the wing and

two elevons, placed at the back of the wing and acting as redundant control surfaces.

We may model the position and attitude of the DarkO by using an inertial reference frame "$[I]$" linked to the earth's surface, and a body reference frame "$[B]$" attached to the drone, with $x_{[B]}$ corresponding to the roll axis (the propellers axes), $y_{[B]}$ being the pitch axis (the direction of the wings) and $z_{[B]}$ being the yaw axis. According to the notation in [5] the left and right propeller/elevon are denoted by using subscripts $i = 1$ (left) and $i = 2$ (right), respectively.

Remark 1: (Plant input saturation) The DarkO actuators have dynamics that limit their actions both in terms of amplitude and rate. For the electric motors generating traction through the propellers, the maximum voltage that can be delivered to the motor and a reasonable low-speed saturation, which is necessary for the plant input transformation introduced in the following (in addition to ensuring a realistic finite energy model), corresponds to constraining $\omega_i \in [200\ ; 2000]\ \mathrm{rad\,s^{-1}}$, $i = 1, 2$. In terms of maximal rate, a reasonable rate saturation level representing the motor actuation chain (consisting of the ESC, the motor and the propeller) corresponds to imposing $\dot{\omega}_i \in [-3000\ ; 3000]\ \mathrm{rad\,s^{-2}}$, $i = 1, 2$, which provides a fairly aggressive actuation system. The saturation levels characterizing the elevons stem from the servo motors type of actuation. The elevons input is limited in displacement by the shape of the UAV and the physical limits of the servo motors, which translates into a saturation of the control surface deflection $\delta_i \in [-30\ ; 30]^\circ$, $i = 1, 2$. Perhaps the most relevant saturation here is the rate phenomenon (due to the servo-motor actuation), which corresponds to $\dot{\delta} \in \{-5.24, 5.24\}\ \mathrm{rad\,s^{-2}}$, $i = 1, 2$ (stemming from a movement of 60° in 0.2 seconds). These saturation levels are only indirectly taken into account in the control design of this paper, but are explicitly considered in our simulation results. ∘

A. Input-affine nonlinear model of DarkO

Since we focus in this paper on the hovering phase, where the speed is small, we may simplify the full nonlinear model (available and described in [18, eqn (2.10), p. 25]) by neglecting the aerodynamic effects, namely all the terms that are quadratic in the speed $\boldsymbol{v_b}$ and $\boldsymbol{\omega_b}$ and the wind effects $\boldsymbol{w}$. Accounting for the wind effects would allow for useful derivations of the linearized dynamics under the wind action, which we regard as future work. Neglecting these terms and performing the following nonlinear input transformation:

$$\boldsymbol{u} := \begin{bmatrix}\tau_1 & \tau_2 & \delta_1\tau_1 & \delta_2\tau_2\end{bmatrix}^\top = k_\mathrm{f}\begin{bmatrix}\omega_1^2 & \omega_2^2 & \delta_1\omega_1^2 & \delta_2\omega_2^2\end{bmatrix}^\top, \quad (1)$$

allows us to derive the following input-affine simplified approximate low-speed model

$$\dot{\boldsymbol{p}} = \boldsymbol{v}, \qquad m\dot{\boldsymbol{v}} = -m\boldsymbol{g} + R(\boldsymbol{q})F\boldsymbol{u}, \quad (2a)$$

$$\dot{\boldsymbol{q}} = \frac{1}{2}\boldsymbol{q} \otimes \boldsymbol{\omega_b}, \qquad J\dot{\boldsymbol{\omega}}_\mathrm{b} = -\left[\boldsymbol{\omega}_\mathrm{b}\right]_\times J\boldsymbol{\omega}_\mathrm{b} + M\boldsymbol{u}, \quad (2b)$$

where $\boldsymbol{p} \in \mathbb{R}^3$ is the position of the center of mass (CoM) expressed in the inertial frame and $\boldsymbol{v} \in \mathbb{R}^3$ denotes its velocity. $\boldsymbol{g} = [0\ 0\ g]^\top$ is the (constant) gravity vector, $\boldsymbol{q}$ is a unit quaternion charactering the attitude and $\boldsymbol{\omega}_\mathrm{b}$ is the rotational speed expressed in the body frame. Finally m is the mass and J is the inertia. The constant matrices F and M can be computed by performing some manipulations of the dynamics, details are available in [18, eqn (2.21), p. 28].

$$F := \begin{bmatrix} a_\mathrm{f} & a_\mathrm{f} & 0 & 0 \\ 0 & 0 & 0 & 0 \\ 0 & 0 & b_\mathrm{f} & b_\mathrm{f} \end{bmatrix}, \; M := \begin{bmatrix} a_\mathrm{m} & -a_\mathrm{m} & b_\mathrm{m} & -b_\mathrm{m} \\ 0 & 0 & c_\mathrm{m} & c_\mathrm{m} \\ d_\mathrm{m} & -d_\mathrm{m} & 0 & 0 \end{bmatrix}, \quad (3)$$

with the following coefficients

$$\left[\begin{array}{c|c} a_\mathrm{f} & b_\mathrm{f} \\ \hline a_\mathrm{m} & b_\mathrm{m} \\ \hline c_\mathrm{m} & d_\mathrm{m} \end{array}\right] = \left[\begin{array}{c|c} 1 - \frac{S}{4S_\mathrm{p}}C_{\mathrm{d}0} & -\frac{S}{4S_\mathrm{p}}(2\pi + C_{\mathrm{d}0})\xi_\mathrm{f} \\ \hline \frac{k_\mathrm{m}}{k_\mathrm{f}} & \frac{S}{4S_\mathrm{p}}a_y(2\pi + C_{\mathrm{d}0})\xi_\mathrm{f} \\ \hline \frac{S}{4S_\mathrm{p}}\Delta_\mathrm{r}(2\pi + C_{\mathrm{d}0})\xi_\mathrm{m} & p_y + \frac{S}{4S_\mathrm{p}}a_y C_{\mathrm{d}0} \end{array}\right],$$

where the numerical values can be found in [18, table 1, p. 61]. Model (2) provides a desirable input-affine description of the DarkO dynamics. Among other things, the simplified nonlinear dynamics (2) allow us to characterize all the possible equilibria induced by input $\boldsymbol{u}$. The corresponding result is formalized next.

Proposition 1: For model (2), all the possible input-state equilibrium pairs $(\boldsymbol{u}, \boldsymbol{x}) = (\boldsymbol{u}_\mathrm{eq}, \boldsymbol{x}_\mathrm{eq}) = (\boldsymbol{u_{eq}}, \boldsymbol{p_{eq}}, \boldsymbol{v_{eq}}, \boldsymbol{q_{eq}}, \boldsymbol{\omega_{b,eq}})$ are parametrized by an arbitrary position $\boldsymbol{p_e} \in \mathbb{R}^3$, and an arbitrary roll orientation $\beta \in \left[-\sqrt{\frac{1}{2}}, \sqrt{\frac{1}{2}}\right]$ as follows

$$\boldsymbol{u}_\mathrm{eq} = \frac{mg}{(1 - \frac{S}{4S_\mathrm{p}}C_{\mathrm{d}0})}[1\ 1\ 0\ 0]^\top \quad (4a)$$

$$\boldsymbol{p_{eq}} = \boldsymbol{p_e}, \quad \boldsymbol{v_{eq}} = 0, \quad \boldsymbol{\omega_{b,eq}} = 0 \quad (4b)$$

$$\boldsymbol{q_{eq}} = [\eta_{eq}\epsilon_{eq}^\top]^\top = \left[\sqrt{\frac{1}{2} - \beta}\ \beta\ \frac{2\beta^2 - 1}{2\sqrt{\frac{1}{2} - \beta}}\ \beta\right]^\top \quad (4c)$$

Proof: To define the equilibrium point, we first set all derivatives to zero. $\boldsymbol{v} = \dot{\boldsymbol{p}} = 0$ and $\dot{\boldsymbol{q}} = \frac{1}{2}\boldsymbol{q} \otimes \boldsymbol{\omega_b} = 0$. Since the norm of the quaternion is unitary, it never vanishes, therefore $\boldsymbol{\omega_b} = 0$, which gives $J\dot{\boldsymbol{\omega}}_\mathrm{b} = M\boldsymbol{u} - [\boldsymbol{\omega_b}]_\times J\boldsymbol{\omega_b} = 0 \implies M\boldsymbol{u} = 0$. Thus, we know that equilibrium is reached when $\boldsymbol{u} \in \ker M$. The basis generating the kernel of M is of the form $[1\ 1\ 0\ 0]^\top$, therefore $\boldsymbol{u} = \lambda[1\ 1\ 0\ 0]^\top$, with $\lambda \in \mathbb{R}$. $m\dot{\boldsymbol{v}} = R(\boldsymbol{q})F\boldsymbol{u} - m\boldsymbol{g} = 0 \implies R(\boldsymbol{q})F\boldsymbol{u} = m\boldsymbol{g}$. Thus the rotation matrix $R(\boldsymbol{q})$, must orient the longitudinal axis of the drone towards the vertical axis to align the forces. The set of quaternions inducing this orientation is $\boldsymbol{q} = \left[\sqrt{\frac{1}{2} - \beta}\ \beta\ \frac{2\beta^2 - 1}{2\sqrt{\frac{1}{2} - \beta}}\ \beta\right]^\top, \ \forall\beta \in \left[-\sqrt{\frac{1}{2}}, \sqrt{\frac{1}{2}}\right]$. Finally, the value of λ that compensates for the gravity is $\lambda = \frac{mg}{(1 - \frac{S}{4S_\mathrm{p}}C_{\mathrm{d}0})}$, as to be proven. ■

We observe that all of the equilibrium pairs characterized in Proposition 1 are associated with a constant control action $\bar{\boldsymbol{u}}$ producing a positive thrust compensating for the gravity effects. In particular, according to the expression of $\boldsymbol{u}_\mathrm{eq}$ in (4a), the necessary thrust corresponds to mg divided by the correction term $(1 - \frac{S}{4S_\mathrm{p}}C_{\mathrm{d}0})^{-1}$, compensating for the aerodynamic losses.

It is interesting to note that, in addition to an arbitrary position $\boldsymbol{p}_e$, we may define an equilibrium exploiting the additional degree of freedom β, characterizing a rotation about the vertical axis of the inertial frame, which is collinear with the longitudinal axis $x_{[B]}$ of the UAV when it is hovering. This degree of freedom is useful, e.g., when wanting to prepare the UAV for a straight flight in a specific direction. Nevertheless, a specific heading must be imposed by the feedback law whenever wanting to reject a constant and nonzero wind disturbance $\boldsymbol{w}$ affecting the dynamics. This type of study is regarded as future work.

B. Linearized dynamics

We derive here the linearized dynamics starting from the simplified nonlinear model (2). Inspired by [19, Proof of Lemma 1], to deal with the dynamics of the quaternion $\boldsymbol{q} = \begin{bmatrix}\eta & \boldsymbol{\epsilon}^\top\end{bmatrix}^\top$ evolving in $\mathbb{S}^3$, we replace η by its nonnegative value induced by the unit norm of the quaternion. Thus, $\eta = (1-\boldsymbol{\epsilon}^\top\boldsymbol{\epsilon})^{\frac{1}{2}} = \sqrt{1-\epsilon_1^2-\epsilon_2^2-\epsilon_3^2}$. The linearized equations of motion are then characterized by the incremental state vector:

$$\begin{aligned}\tilde{\boldsymbol{x}} &:= \begin{bmatrix}\tilde{\boldsymbol{p}} & \tilde{\boldsymbol{v}} & \tilde{\boldsymbol{\epsilon}} & \tilde{\boldsymbol{\omega}}_{\boldsymbol{b}}\end{bmatrix}^\top \qquad \tilde{\boldsymbol{u}} := \boldsymbol{u} - \boldsymbol{u}_{\boldsymbol{eq}} \quad (5)\\ &:= \begin{bmatrix}\boldsymbol{p}-\boldsymbol{p}_{eq} & \boldsymbol{v} & \boldsymbol{\epsilon}-\boldsymbol{\epsilon}_{eq} & \boldsymbol{\omega}_{\boldsymbol{b}}\end{bmatrix}^\top,\end{aligned}$$

where the constants $\boldsymbol{p}_{eq} \in \mathbb{R}^3$, $\boldsymbol{u}_{eq} \in \mathbb{R}^4$ and $\boldsymbol{\epsilon}_{eq} \in \mathbb{R}^3$ come from any of the equilibrium pairs characterized in Proposition 1.

We may then characterize the linearized dynamics about any such equilibrium pair as follows

$$\dot{\tilde{\boldsymbol{x}}} = A\tilde{\boldsymbol{x}} + G\tilde{\boldsymbol{u}} \tag{6}$$

where the expression of A, can be determined, after some manipulations, as

$$A = \begin{bmatrix}\mathbb{0}_3 & \mathbb{I}_3 & \mathbb{0}_3 & \mathbb{0}_3\\ \mathbb{0}_3 & \mathbb{0}_3 & A_{\dot{v},\epsilon} & \mathbb{0}_3\\ \mathbb{0}_3 & \mathbb{0}_3 & \mathbb{0}_3 & A_{\dot{q},\omega_\mathrm{b}}\\ \mathbb{0}_3 & \mathbb{0}_3 & \mathbb{0}_3 & \mathbb{0}_3\end{bmatrix} \begin{matrix} A_{\dot{q},\omega_\mathrm{b}} = \frac{\sqrt{2}}{4}\begin{bmatrix}1 & 0 & -1\\ 0 & 1 & 0\\ 1 & 0 & 1\end{bmatrix}\\ A_{\dot{v},\epsilon} = \sqrt{2}\begin{bmatrix}0 & 2g & 0\\ -g & 0 & g\\ 0 & -g & 0\end{bmatrix}\end{matrix} \tag{7}$$

In matrix A, we thus obtain a pure integrator on the first three rows of the matrix of the equation (7), which represents the link between the velocity and the linear acceleration. We observe that the linear acceleration depends only on the orientation of the UAV. This orientation is only dependent on the angular velocity, while the angular velocities are not affected by the state vector, as one may expect.

The expression of G can be determined following similar derivations, and corresponds to

$$G = \begin{bmatrix}\mathbb{0}_{3\times1} & \mathbb{0}_{3\times1} & \mathbb{0}_{3\times1} & \mathbb{0}_{3\times1}\\ 0 & 0 & a_\mathrm{g} & a_\mathrm{g}\\ 0 & 0 & 0 & 0\\ b_\mathrm{g} & b_\mathrm{g} & 0 & 0\\ \mathbb{0}_{3\times1} & \mathbb{0}_{3\times1} & \mathbb{0}_{3\times1} & \mathbb{0}_{3\times1}\\ c_\mathrm{g} & -c_\mathrm{g} & d_\mathrm{g} & -d_\mathrm{g}\\ 0 & 0 & e_\mathrm{g} & e_\mathrm{g}\\ f_\mathrm{g} & -f_\mathrm{g} & 0 & 0\end{bmatrix},$$

with

$$\left[\begin{array}{c|c} a_\mathrm{g} & b_\mathrm{g}\\ \hline c_\mathrm{g} & d_\mathrm{g}\\ \hline e_\mathrm{g} & f_\mathrm{g}\end{array}\right] = \left[\begin{array}{c|c} \frac{S}{4mS_\mathrm{p}}(2\pi + C_{\mathrm{d}0})\xi_\mathrm{f} & \frac{1}{m}(1-\frac{S}{4S_\mathrm{p}}C_{\mathrm{d}0})\\ \hline \frac{J_1 k_\mathrm{m}}{k_\mathrm{f}} & \frac{a_y}{J_1}(2\pi + C_{\mathrm{d}0})\xi_\mathrm{m}\\ \hline \frac{S\Delta_\mathrm{r}}{4J_2S_\mathrm{p}}(2\pi + C_{\mathrm{d}0})\xi_\mathrm{m} & \frac{1}{J_3}(p_y + \frac{S}{4S_\mathrm{p}}a_y C_{\mathrm{d}0})\end{array}\right].$$

From an actuation point of view, we observe in the linearized model that the input $\tilde{\boldsymbol{u}}$ only acts on the acceleration of the UAV. Moreover, the input matrix G shows that it is not possible to generate any acceleration along the y_b axis, which is reasonable, given the architecture of the DarkO UAV.

III. Feedback control design

We derived in Section II the simplified nonlinear model (2), which presents a convenient input-affine relation with respect to $\boldsymbol{u}$, and the linearized dynamics about the equilibria, represented by (6).

We propose in this section two control design strategies for stabilizing a hovering position. The first one is inspired by the nonlinear stabilizer presented in [20] and provides a large region of attraction, and the second one is based on the linearized dynamics and allow for more effective gain tuning in the final approaching phase. The two controllers are united via a hybrid mechanism that allows retaining the steady-state performance of the linearized design with the large region of attraction guaranteed by the nonlinear design. Our solution is tested by simulating the full nonlinear model.

Remark 2: We emphasize that vector $\boldsymbol{u}$ in (1) corresponds to a non-invertible transformation of the actual DarkO actuators corresponding to $\boldsymbol{u}_{\text{act}} := [\omega_1,\ \omega_2,\ \delta_1,\ \delta_2]^\top$. Nevertheless, when imposing the saturation constraints discussed in Remark 1, it is possible to uniquely determine $\boldsymbol{u}_{\text{act}}$ from a desired value of $\boldsymbol{u}$ in (1), because nonzero positive values of ω_1 and ω_2 can be determined from the first two components of $\boldsymbol{u}$, and then δ_1 and δ_2 are easily constructed from the last two components of $\boldsymbol{u}$. ∘

A. Nonlinear dynamic feedback controller

We illustrate in this section a nonlinear dynamic control law inspired by the result of [20]. For the nonlinear control law of [20] to be applicable, matrices F and M reported in (3) must allow defining a so-called zero moment direction $\bar{\boldsymbol{u}} \in \mathbb{R}^4$ ensuring $|F\bar{\boldsymbol{u}}| = 1$ and $M\bar{\boldsymbol{u}} = 0$, and a right inverse M^r of M satisfying $MM^r = I$ and $FM^r = 0$. In our case, it is immediate to see that the zero-moment direction $\bar{\boldsymbol{u}} = \frac{\sqrt{2}}{2a_\mathrm{f}}\begin{bmatrix}1 & 1 & 0 & 0\end{bmatrix}^\top$ satisfies the required conditions, whereas the fact that $\mathrm{rank}(F) = 2$ (so that $\ker F$ has dimension 2) makes it impossible to find a right inverse M^r of M completely contained in $\ker F$. Due to this fact, we determine M^r by (conservatively) parametrizing the right pseudoinverses of M as $M^r := KM^\top(MKM^\top)^{-1}$ where parameter $K \in \mathbb{R}^{4\times4}$ is symmetric and satisfies $MKM^\top \geq I$ (to ensure invertibility). Under this parametrization, the goal is to minimize the norm of $FM^r = FKM^\top(MKM^\top)^{-1}$, which is well achieved by minimizing the norm of $FKM^\top$, due to the fact that the constraint on $MKM^\top \geq I$ ensures that the factor $(MKM^\top)^{-1}$ has norm smaller than 1. Performing

a Schur complement, this minimization is well obtained by solving the following semi-definite program:

$$\min_{K,\kappa} \kappa, \text{ subject to: } MKM^\top \geq I, \begin{bmatrix} \kappa I & FKM^\top \\ MK^\top F^\top & \kappa I \end{bmatrix} \geq 0,$$

which minimizes κ while ensuring $FKM^\top MK^\top F^\top \leq \kappa^2 I$. Solving this optimization, we obtain, for the specific matrices under consideration,

$$K = \begin{bmatrix} 0 & -737 & 171 & -171 \\ -737 & 0 & -171 & 171 \\ 171 & -171 & 1583.5 & -43.73 \\ -171 & 171 & -43.73 & 1583.5 \end{bmatrix}, \; M^r = \begin{bmatrix} 0 & 0 & -3.19 \\ 0 & 0 & 3.19 \\ -4.51 & -27.75 & -1.48 \\ 4.51 & -27.75 & 1.48 \end{bmatrix}$$

leading to $\kappa = 39.7$. With this optimality-based selection, the nonlinear dynamic design of [20] can be effectively applied by obtaining responses that are almost indistinguishable from the fully decoupled case $FM^r = 0$. Note that a similar approach, essentially neglecting the extra terms acting on the translational dynamics is also suggested in the survey paper [4].

Based on the above-described choice of M^r and $\bar{\boldsymbol{u}}$, applying the feedback law in [20, eqn (19)], the input $\boldsymbol{u}$ becomes :

$$\boldsymbol{u} = \boldsymbol{u}_{\text{nl}} := M^r \boldsymbol{\tau_r} + \bar{\boldsymbol{u}} \boldsymbol{f}, \tag{8}$$

where $\boldsymbol{\tau_r}$ and $\boldsymbol{f}$ are provided by the dynamic feedback controller proposed in [20].

The optimality-based selection of M^r is prone to a few interesting interpretations when observing the product $M^r \boldsymbol{\tau_r} = M^r \begin{bmatrix} \tau_{r,x} & \tau_{r,y} & \tau_{r,z} \end{bmatrix}^\top$. First, to produce a moment $\tau_{r,z}$ about the z-axis we mainly use the thrust differential action; secondly, a moment $\tau_{r,y}$ about the y-axis is generated by an equal (additive) use of the two flaps, with great efficiency; finally a moment $\tau_{r,x}$ about the x-axis comes from a differential use of the flaps.

As a final remark, as compared to the solution proposed in [20], to partially take into account the saturation effects highlighted in Remark 1, the error feedback interconnection of the outer loop in [20] has been augmented with a simple error governor strategy never allowing the translational position error $\mathbf{e}_p$ entering [20, eqn. (22)] to exceed the maximum value of 3 meters. The remaining tuning gains required in the solution of [20] have been selected following an intuitive PD tuning procedure as $k_{pp} = 0.5$, $k_{pd} = 1.2$, $k_{ap} = 0.08$, $k_{ad} = 0.1$ and $k_\Delta = 1$.

Figure 1 shows the response of the system in terms of linear and angular positions (top two rows) and actuators efforts (bottom two rows) when the system starts from the initial condition $\boldsymbol{x(0)} = [\boldsymbol{p(0)} \; \boldsymbol{v(0)} \; \boldsymbol{q(0)} \; \boldsymbol{\omega_b(0)}]^\top = [0 \; 0 \; 0 \; 0 \; 0 \; 0 \; 0.9140 \; 0.1134 \; -0.3728 \; 0.1134 \; 0 \; 0 \; 0]^\top$ with a target equilibrium position of $\boldsymbol{p}_{\text{eq}} = [4 \; 5 \; 6]^\top$ and $\boldsymbol{q}_{\text{eq}} = [\frac{\sqrt{2}}{2} \; 0 \; -\frac{\sqrt{2}}{2} \; 0]^\top$. A graceful response can be seen, which remains quite far from the actuator saturations (see Remark 1). Increasing the tuning gains can speed up the response but provides undesired attitude oscillations. Therefore it is interesting to combine this nonlinear controller (providing a large region of attraction) with a more aggressive controller, designed based on the linearized dynamics (6) and to be used to improve the fail of the response.

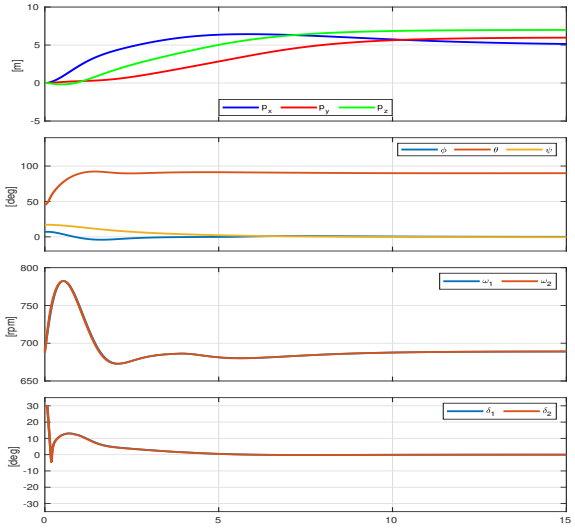

Fig. 1. Simulation with the nonlinear dynamic feedback controller.

B. Linear control design

Based on the performance-oriented observations of the previous section, given a target position corresponding to an equilibrium $\boldsymbol{p}_{\text{eq}}, \boldsymbol{q}_{\text{eq}}$ as characterized in Proposition 1, we design here a local linear feedback controller capable of inducing a more aggressive response. To this end, we focus on the linearized dynamics (6) and recognize that we can design a state feedback controller

$$\boldsymbol{u}_{\text{lin}} := \boldsymbol{u}_{\text{eq}} - K\tilde{\boldsymbol{x}}, \tag{9}$$

where $\tilde{\boldsymbol{x}}$ has been introduced in (5) and $K \in \mathbb{R}^{4\times 12}$ is a state feedback gain that can be designed, based on the matrices A and G appearing in (6), in such a way that the closed-loop linear feedback $A_{\text{cl}} := A - GK$ be exponentially stable.

For our design, we have used an LQR selection, associated with the simplest possible weight matrices selection $Q = I_{12}$ and $R = I_4$, which gives desirable closed-loop responses. The LQR design also provides a positive definite Lyapunov certificate matrix $S \in \mathbb{R}^{12\times 12}$ (solution of the algebraic Riccati equation) ensuring that $A_{\text{cl}}^\top S + S A_{\text{cl}} < 0$. In particular, it is well known from the linear approximation theorem that function $V(\tilde{\boldsymbol{x}}) = \tilde{\boldsymbol{x}}^\top S \tilde{\boldsymbol{x}}$ is also a Lyapunov function certifying local exponential stability of $\boldsymbol{x_{\text{eq}}}$ for the nonlinear dynamics. More specifically, there exits a positive scalar $\bar{v} \in \mathbb{R}$ such that, along dynamics (2), we have :

$$V(\tilde{\boldsymbol{x}}) \leq \bar{v} \quad \Rightarrow \quad \dot{V}(\tilde{\boldsymbol{x}}) := \langle \nabla V(\tilde{\boldsymbol{x}}), \dot{\tilde{\boldsymbol{x}}} \rangle < 0, \tag{10}$$

for all $\tilde{\boldsymbol{x}} \neq 0$; in other words, the sublevel set $V(\tilde{\boldsymbol{x}}) \leq \bar{v}$ is contained in the basin of attraction of the equilibrium $\boldsymbol{x}_{\text{eq}}$.

Determining the largest possible scalar $\bar{v}$ ensuring (10) is a challenging problem and conservative lower bounds of this quantity can be determined by quantifying the effect of the nonlinearities on the dynamics. Since $\dot{\tilde{\boldsymbol{x}}}$ is a function of $\boldsymbol{x}$, then it is fairly easy to algebraically evaluate $\dot{V}(\tilde{\boldsymbol{x}})$ for a large amount of random extractions of the variable $\tilde{\boldsymbol{x}}$, so as to get a probabilistic estimate of the largest $\bar{v}$. Rigorous guarantees about these selections can be obtained

by applying the results in [21], which is out of the scope of this paper, but an evaluation of 10000 samples confirmed that the value $\bar{v} = 400$ is a good candidate selection satisfying (10).

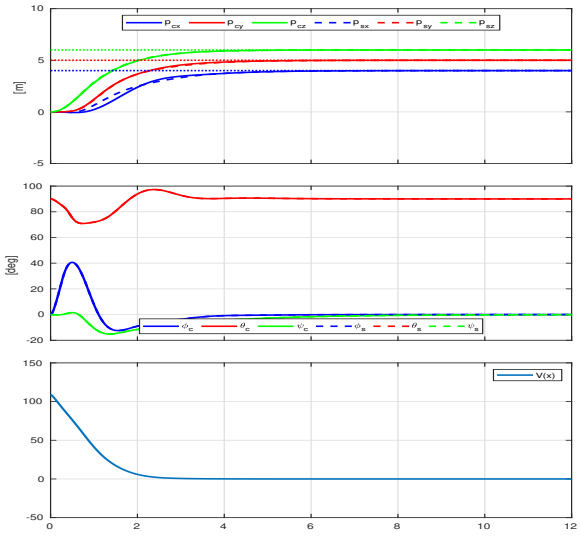

Fig. 2. Simulation of the full model (solid) and (2) (dashed) with $\boldsymbol{u} = \boldsymbol{u}_{\text{lin}}$ as in (9) from an initial condition $\tilde{\boldsymbol{x}}_{\boldsymbol{0}}$ within the basin of attraction.

Figure 2 shows a simulation starting at the origin with a zero orientation on the three axes (horizontal UAV) and zero initial velocities, with a target position $\boldsymbol{p}_{\text{eq}} = [4,\ 5,\ 6]$ with a hovering stabilization (vertical UAV) with $\beta = 0$. The dotted line represents the target position on each axis. Note that the initial linear and angular velocities are zero. The last graph shows the desirable exponential decay of V. Figure 2 shows both the simulation of the full model (solid) of [18] and of the simplified nonlinear model (2) (dashed) showing some significant differences in the initial response. When providing a larger target position $\boldsymbol{p}_{\text{eq}} = [8,\ 9,\ 10]$ (with the same orientation), the initial condition is outside the basin of attraction and diverging solutions are experienced as shown in Figure 3.

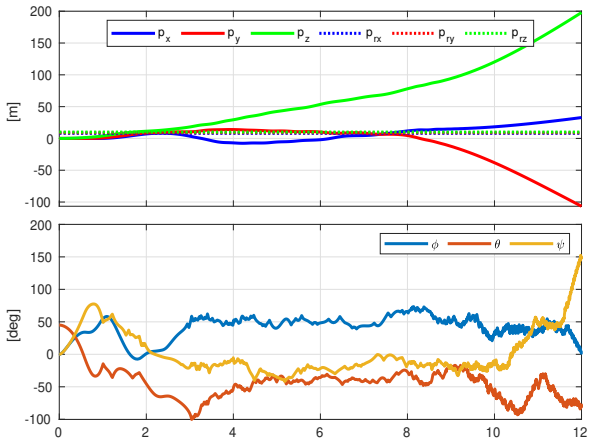

Fig. 3. Diverging simulation of the full model with $\boldsymbol{u} = \boldsymbol{u}_{\text{lin}}$ as in (9) from an initial condition $\tilde{\boldsymbol{x}}_{\boldsymbol{0}}$ outside the basin of attraction.

C. Hysteresis-based local-global control design

Inspired by the local/global strategies presented in [22, Ex. 1.7], similar to the solution presented in [23], we use a hybrid mechanism to switch between the high performance local feedback (9) (as long as the state is in the basin of attraction of the equilibrium) and the less aggressive nonlinear controller (8), which provides a larger region of attraction (and can be called with an abuse of notation the "global controller"). To this end, we augment the controller state with a logical state variable $\ell \in \{0, 1\}$, governing the choice of the control input between (8) and (9) as

$$\boldsymbol{u} = \boldsymbol{u}_{\text{hyb}} := \ell \boldsymbol{u}_{\text{nl}} + (1 - \ell)\boldsymbol{u}_{\text{lin}}, \tag{11}$$

We ensure, through the hybrid dynamics, that ℓ can only take values in $\{0, 1\}$. Its dynamics is defined by:

$$\begin{cases} \dot{\ell} = 0, & \chi \in \mathcal{C} \\ \ell^{+} = 1 - \ell, & \chi \in \mathcal{D} \end{cases}$$

where $\chi = [\boldsymbol{p},\ \boldsymbol{v},\ \boldsymbol{q},\ \boldsymbol{\omega},\ l]$ is the complete closed loop state and $\mathcal{C}$ and $\mathcal{D}$ are, respectively, the flow and the jump sets, defined as

$$\begin{aligned} &\mathcal{C} := \mathcal{C}_0 \cup \mathcal{C}_1,\ \mathcal{D} := \mathcal{D}_0 \cup \mathcal{D}_1, \\ &\mathcal{C}_0 := \{\boldsymbol{\chi} \in \mathbb{R}^{14} :\ V(\tilde{\boldsymbol{x}}) \leq \overline{v} \text{ and } \ell = 0\} \\ &\mathcal{C}_1 := \left\{\boldsymbol{\chi} \in \mathbb{R}^{14} :\ V(\tilde{\boldsymbol{x}}) \geq \underline{v} \text{ and } \ell = 1\right\} \\ &\mathcal{D}_0 := \left\{\boldsymbol{\chi} \in \mathbb{R}^{14} :\ V(\tilde{\boldsymbol{x}}) \geq \overline{v} \text{ and } \ell = 0\right\} \\ &\mathcal{D}_1 := \left\{\boldsymbol{\chi} \in \mathbb{R}^{14} :\ V(\tilde{\boldsymbol{x}}) \leq \underline{v} \text{ and } \ell = 1\right\} \end{aligned}$$

where $V(\tilde{\boldsymbol{x}}) := \tilde{\boldsymbol{x}}^{\top} S \tilde{\boldsymbol{x}}$ has been defined in the previous section, $\overline{v} = 400$ has been determined in the previous section to satisfy (10), and $\underline{v}$ is any positive constant satisfying $\underline{v} < \overline{v}$ (a smaller choice of $\underline{v}$ increases the hysteresis margin but postpones the desirable high performance tail of the feedback response). In our case we choose $\underline{v} = 350$. The following result is an immediate consequence of the results in [22, Ex. 1.7] and the properties of our linear and nonlinear designs.

Proposition 2: Under the action of the hybrid feedback (11), the closed loop exhibits the same basin of attraction as the one associated with the nonlinear controller (8), while always using the high-performance linear feedback (9) in the tail of the response.

We performed several simulations of the closed loop using the Matlab toolbox [24]. The simulations are carried out with the complete model of the UAV [18], including all the nonlinear aerodynamic effects. A sample simulation is reported in Figure 4, where we initialize the UAV at the origin with zero roll and yaw orientation, and with a pitch angle of 45 degrees. The target orientation is in the vertical hovering configuration and the target position is assigned to $\boldsymbol{p}_{\text{eq}} = [50,\ 25,\ 12.5]$. We observe that in the time phase $t \in [0, 38]$, the UAV exhibits a graceful but slow convergence to the desired target position using the global controller ($\ell = 1$). At that time, the state enters set $\mathcal{D}_1$ and the more aggressive local controller is activated up to the convergence to the desired equilibrium.

To perform realistic simulations, the measurements are affected by sensors noise. The intrinsic robustness of the hybrid feedback, established in [22, Chapter 7] is confirmed by the graceful performance degradation as a function of the amplitude of the measurement noise.

ACKNOWLEDGMENT

The authors would like to thank Gautier Hattenberger, Murat Bronz and Jean-Philippe Condomines for useful discussions.

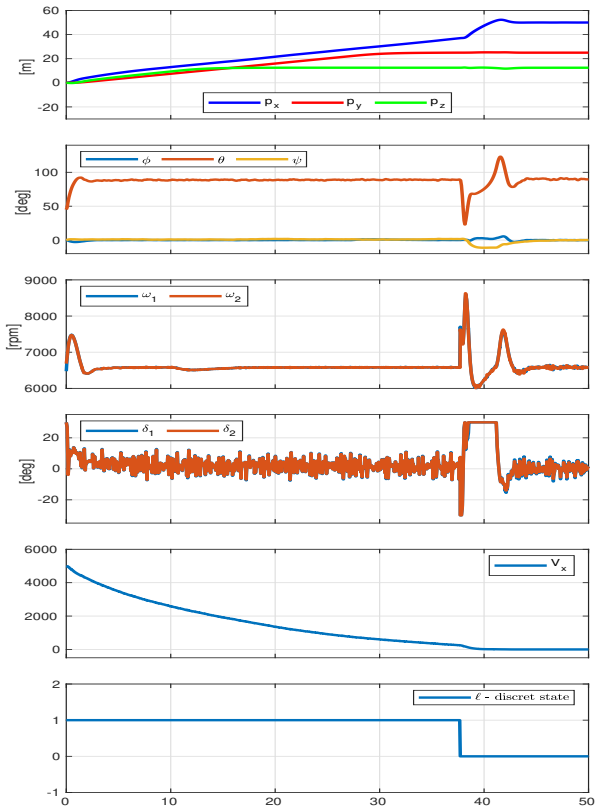

Fig. 4. Closed-loop simulation with the hybrid controller (11).

IV. Conclusions and Future Work

We presented two simplified models of the DarkO UAV that are useful for hovering control design. First, an input-affine nonlinear model allows adopting a nonlinear hierarchical stabilizing feedback. Then, a linearized model allows designing a simple state-feedback solution inducing desirable performance but a small basin of attraction. A hybrid control solution based on a hysteresis mechanism allows combining these two approaches. Future work will include accounting for the effect of the wind. In particular, extending our simplified input-affine model to consider the wind effect is straightforward, while studying perturbed linearized motion is currently under investigation. Future work also includes experimental validation of our control laws in the ENAC flight arena, in addition to generalizing the hovering stabilization solutions to the more challenging trajectory tracking problem.

References

[1] A. Saeed, A. Younes, C. Cai, and G. Cai, "A survey of hybrid unmanned aerial vehicles," *Progress in Aerospace Sciences*, vol. 98, pp. 91–105, 2018.

[2] J. M. Olszanecki Barth, J.-P. Condomines, M. Bronz, J.-M. Moschetta, C. Join, and M. Fliess, "Model-free control algorithms for micro air vehicles with transitioning flight capabilities," *International Journal of Micro Air Vehicles*, vol. 12, pp. 1–22, Apr. 2020.

[3] N. Hegde, V. George, C. Nayak, and A. Vaz, "Application of robust h-infinity controller in transition flight modeling of autonomous VTOL convertible quad tiltrotor UAV," *International Journal of Intelligent Unmanned Systems*, 2021.

[4] M.-D. Hua, T. Hamel, P. Morin, and C. Samson, "Introduction to feedback control of underactuated vtol vehicles: A review of basic control design ideas and principles," *Control Systems, IEEE*, vol. 33, pp. 61–75, 02 2013.

[5] L. R. Lustosa, F. Defaÿ, and J.-M. Moschetta, "Global Singularity-Free Aerodynamic Model for Algorithmic Flight Control of Tail Sitters," *Journal of Guidance, Control, and Dynamics*, vol. 42, no. 2, pp. 303–316, Feb. 2019.

[6] L. Lustosa, F. Defaÿ, and J. Moschetta, "Longitudinal study of a tilt-body vehicle: modeling, control and stability analysis," in *Proc. of International Conference on Unmanned Aircraft Systems*, Denver, Colorado, US, June 2015, pp. 816–824.

[7] J. Escareno, R. Stone, A. Sanchez, and R. Lozano, "Modeling and control strategy for the transition of a convertible tail-sitter UAV," in *European Control Conference*, 2007, pp. 3385–3390.

[8] J. Forshaw, V. Lappas, and P. Briggs, "Transitional control architecture and methodology for a twin rotor tailsitter," *AIAA Journal of Guidance, Control, and Dynamics*, vol. 37, no. 4, pp. 1289–1298, 2014.

[9] D. Liu, H. Liu, Z. Li, X. Hou, and Q. Wang, "Robust attitude control for tail-sitter unmanned aerial vehicles in flight mode transitions," *International Journal of Robust and Nonlinear Control*, vol. 29, no. 4, pp. 1132–1149, 2019.

[10] D. Chu, J. Sprinkle, R. Randall, and S. Shkarayev, "Simulator development for transition flight dynamics of a vtol mav," *International Journal of Micro Air Vehicles*, vol. 2, no. 2, pp. 69–89, 2010.

[11] C. Chen, J. Zhang, D. Zhang, and L. Shen, "Control and flight test of a tilt-rotor unmanned aerial vehicle," *International Journal of Advanced Robotic Systems*, vol. 14, no. 1, p. 1729881416678141, 2017.

[12] E. J. J. Smeur, M. Bronz, and G. C. H. E. de Croon, "Incremental control and guidance of hybrid aircraft applied to the Cyclone tailsitter UAV," *Journal of Guidance, Control, and Dynamics*, Sep. 2019.

[13] G. Di Francesco and M. Mattei, "Modeling and incremental nonlinear dynamic inversion control of a novel unmanned tiltrotor," *AIAA Journal of Aircraft*, vol. 53, no. 1, pp. 73–86, 2016.

[14] N. Silva, J. Fontes, R. Inoue, and K. Branco, "Dynamic inversion and gain-scheduling control for an autonomous aerial vehicle with multiple flight stages," *Journal of Control, Automation and Electrical Systems*, vol. 29, no. 3, pp. 328–339, 2018.

[15] N. Slegers, J. Kyle, and M. Costello, "Nonlinear model predictive control technique for unmanned air vehicles," *AIAA Journal of guidance, control, and dynamics*, vol. 29, no. 5, pp. 1179–1188, 2006.

[16] S. Swarnkar, H. Parwana, M. Kothari, and A. Abhishek, "Biplane-quadrotor tail-sitter UAV: Flight dynamics and control," *AIAA Journal of Guidance, Control, and Dynamics*, vol. 41, no. 5, pp. 1049–1067, 2018.

[17] A. Marcos and G. Balas, "Development of linear-parameter-varying models for aircraft," *AIAA Journal of Guidance, Control, and Dynamics*, vol. 27, no. 2, pp. 218–228, 2004.

[18] F. Sansou, "Commande hybride d'un drone convertible pour des déplacements sous optimaux," 2022. [Online]. Available: https://arxiv.org/abs/2203.15387

[19] J.-F. Tregouet, D. Arzelier, D. Peaucelle, C. Pittet, and L. Zaccarian, "Reaction Wheels Desaturation Using Magnetorquers and Static Input Allocation," *IEEE Transactions on Control Systems Technology*, vol. 23, no. 2, pp. 525 – 539, Feb. 2015.

[20] G. Michieletto, A. Cenedese, L. Zaccarian, and A. Franchi, "Hierarchical nonlinear control for multi-rotor asymptotic stabilization based on zero-moment direction," *Automatica*, vol. 117, p. 108991, 2020.

[21] R. Tempo, G. Calafiore, and F. Dabbene, *Randomized algorithms for analysis and control of uncertain systems: with applications*. Springer, 2013.

[22] R. Goebel, R. G. Sanfelice, and A. R. Teel, *Hybrid Dynamical Systems: Modeling, Stability, and Robustness*. New Jersey: Princeton University Press, 2012.

[23] M. Andreetto, D. Fontanelli, and L. Zaccarian, "Quasi time-optimal hybrid trajectory tracking of an n-dimensional saturated double integrator," in *IEEE Conference on Control Applications*, 2016, pp. 550–555.

[24] R. Sanfelice, D. Copp, and P. Nanez, "A toolbox for simulation of hybrid systems in matlab/simulink: Hybrid equations (HyEQ) toolbox," pp. 101–106, 2013.